A comparative study of the dissolution mechanisms of amorphous and crystalline feldspars at acidic pH conditions

Benjamin Cagnon, Damien Daval, Martiane Cabié, Damien Lemarchand, Stéphane Gin

ARTICLE OPEN

Check for updates

A comparative study of the dissolution mechanisms of amorphous and crystalline feldspars at acidic pH conditions

Benjamin Cagnon[1,2]✉, Damien Daval[1,2], Martiane Cabié[3], Damien Lemarchand[1] and Stéphane Gin[4]

The dissolution of amorphous and crystalline oligoclase, a Na-feldspar with traces of Ca and K, was investigated at 90 °C and acidic pH of 1.5 and 3 to unravel the impact of long- and short-range orders on silicate dissolution mechanisms. Experiments were conducted in solutions spiked with $^{29}SiO_2$(aq) and saturated with respect to SiO_2(am). Through morphology, structural, and composition characterizations, we showed that on the amorphous samples (glass samples), the altered layer was mostly formed by leaching, while a combination of both interfacial precipitation and leaching explains the layers formed on the crystalline sample. As expected, the altered layer was thicker at the most acidic pH and it became passivating on crystalline sample at pH 3. The alteration was faster on amorphous oligoclase than on its crystalline equivalent due to the more open structure of the glass. The preferential release of Al was suggested to play a key role, by weakening the silicate network of both substrates. Finally, in this study, a large overestimation of the global alteration of the materials was noticed based on the solution analyses. Discrepancies with solid analyses were attributed to an underestimation (≥2-fold factor) of the total reactive surface area.

npj Materials Degradation (2022)6:34 ; https://doi.org/10.1038/s41529-022-00240-6

INTRODUCTION

Silicates represent the most abundant group of minerals on Earth. They can also be amorphous, such as those found on the seafloor, under the form of silicate glass. Silicate minerals and glasses are structurally different, leading to a different reactivity with water. Both are made of the same structural units (for instance, SiO_4^{4-} or AlO_2^- tetrahedrons) but with varying bond lengths and angles between them, yielding some disorder at short range. At longer distance (>1–5 nm), silicate glasses are generally homogeneous. The structural disorder in glass results in a broad distribution of the dissolution- rate parameters and associated bond-dissociation activation energies. Conversely, minerals are ordered at both short and long distances, meaning that a limited number of atomic bond lengths and angles is found periodically in the structure. In turn, the long-range order shapes crystal habit and the reactivity of individual crystal faces[1].

Understanding the aqueous reactivity of silicates is important as they are involved in fundamental processes such as the biogeochemical cycle of elements[2], as well as industrial processes such as carbon dioxide (CO_2) sequestration[3] and vitrified nuclear waste disposal[4–6] among others.

Historically, several mechanisms have been suggested to take place in parallel and control aluminosilicate glass dissolution:

(1) Diffusion of water into the glass through the largest silicate rings[7], resulting in an exchange between dissociated water and alkali atoms near nonbridging oxygen (NBO) atoms, and the formation of silanol groups[8]. These simultaneous processes, also called interdiffusion, result in the formation of a distinct layer from the parent glass. This layer can be revealed from its porous texture, amorphous structure[9,10], and its chemical composition depleted in glass modifiers (such as Na) and potentially enriched in exogenous elements (H^+, Li^+, or other elements from the solution)[11]. Such reactions are favored at acid pH.

(2) Matrix dissolution, leading to a progressive depolymerization of the structure through hydrolysis of Si–O–M (M = Si, Al, or other glass formers) linkages[12]:

$$\equiv Si - O - Si \equiv + H_2O \rightarrow 2 \equiv Si - OH \quad (1)$$

As long as the solution remains far from the equilibrium, Si is released into the solution at a constant rate called initial or forward rate. This rate is pH- and temperature-dependent[13]. When the concentration of H_4SiO_4(aq) increases, backward reactions of condensation of silanol groups take place at the glass surface, leading to the formation of a porous and hydrated material, called gel layer[14,15].

In this regime, the glass dissolution rate can drop by several orders of magnitude as compared with the initial dissolution rate[16]. This decrease in glass reactivity results both from the reduced affinity of the dissolution reaction of silicate network[17], and the transport-limiting properties of the growing gel layer[18–21]. In the first case, the concentration of glass elements increases in the solution and when it reaches a steady state with the material, the thickness of the gel layer would remain constant. However, the gel layer is not in equilibrium with the solution and evolves over time[21,22]: reorganization and densification of the gel occur gradually, resulting from the condensation of silanol groups into siloxane bonds[23,24]. With the second process, because of the closure of the pores, the transport properties of the surface layer between the glass and the bulk solution are hindered, explaining the observed drop in the dissolution rate[25]. The resulting dissolution is then controlled by the concentration of H_4SiO_4(aq) in the solution, which affects the distance from equilibrium at the interface between the gel layer and the solution[26].

(3) Once steady state is achieved, glass dissolution continues at a slow and near-constant rate called "residual rate" or "final rate". The origin of this residual rate has been discussed in a

[1]Université de Strasbourg/CNRS/ENGEES, ITES, Strasbourg, France. [2]Univ. Grenoble Alpes, Univ. Savoie Mont Blanc, CNRS, IRD, IFSTTAR, ISTerre, Grenoble, France. [3]Aix Marseille Univ, CNRS, Centrale Marseille, FSCM, CP2M, Marseille, France. [4]CEA, DEN, DE2D, University of Montpellier, Marcoule, France. ✉email: benjamin.cagnon@univ-grenoble-alpes.fr

recent article[27,28]. Globally, it is to be attributed to the absence of thermodynamic equilibrium between the glass, the gel, and the solution, although the latter can be highly concentrated in glass constituents. These conditions favor the precipitation of secondary phases, which, in turn, can impact the solution chemistry. The secondary phases first precipitate following heterogeneous nucleation at the interface between the solution and the gel layer. In circum-neutral to mildly basic conditions (pH 6–9), mainly phyllosilicates precipitate, while in basic condition (pH >10), zeolite (among other silicate minerals) may form. The precipitation of secondary phases can trigger the resumption of glass alteration[29–33].

Historically, the leaching process described in (1) was supposed to apply to silicate minerals as well[34,35]. Using spectroscopic techniques, Hellmann et al.[36], demonstrated the formation of layers enriched in H and depleted in Na at the surface of dissolved albite ($NaAlSi_3O_8$). The depth profiles of these elements were found to be sigmoidal and anticorrelated, leading the authors to suggest that the layers form through an interdiffusion mechanism, similarly to glass alteration. However, these diffusion profiles have been challenged in subsequent studies, which suggested that they represent an analytical artifact resulting from the poor lateral resolution of the ion or X-ray beam measurements. Instead, more recent results concluded to profiles with step-like functions[37]. Diffusion models fail to predict such observations[37–39], pointing out that the reaction is not diffusion-controlled. In addition, the sharp structural transition between the crystalline (mineral) and the amorphous (altered layer) zones is at odds with a diffusion-controlled leaching process.

Following the early conclusion of Hellmann et al.[37], a growing number of studies[40–44] has subsequently supported another mechanism. Whereas the leached-layer mechanism suggests that the altered layer represents a relict structure of the primary silicate (formed via hydrolysis–condensation reactions with no detachment of Si from the glass network), this alternative mechanism, called coupled interfacial dissolution–reprecipitation (CIDR), suggests that all Si–O bonds are broken simultaneously to release Si atoms to the interfacial solution. Hellmann et al.[39], suggested that the mineral dissolves congruently in a thin water film in contact with its surface. In this thin water film, the concentration of H_4SiO_4(aq) becomes supersaturated with respect to amorphous silica, leading to the precipitation of porous amorphous silica — the so-called altered layer, distinct from the mineral. The remaining elements then diffuse through the nanoporosity of the reprecipitated layer[42]. The formation and densification (due to local chemical composition, local concentration gradient, and local diffusivity and porosity) of the altered layer may control the temporal decrease of silicate dissolution rate, as suggested by Daval et al.[45] for wollastonite.

Recently, a study conducted by Hellmann et al.[46], suggested that the CIDR mechanism could also apply to glass alteration. Confirming the results of Geisler et al.[40], Hellmann et al.[46], evidenced (i) a sharp interface between the pristine glass and the altered layer, (ii) nm-wide concentration gradient in the solid materials, and (iii) a thickness of altered layer, which is, as diffusion profiles, independent of the charge of cation (usually, the cationic charge is negatively correlated with the diffusion length). Conversely, Gin et al.[47] used atom-probe tomography to prove the existence of such gradients and demonstrated that depending on the presence of Al in the glass, alteration can proceed following the leaching mechanism or the CIDR mechanism[48].

In order to predict and model the behavior of glass and mineral dissolution, it is therefore important to develop a unified approach that overcomes the opposition between the two mechanisms. In a recent study, Pérez et al.[1] investigated the dissolution mechanisms of oligoclase glass and its crystalline equivalent over a wide range of pH. Whereas for the crystalline materials, altered layers likely formed following the CIDR mechanism, conversely, the altered layer developed on oligoclase glass was suggested to form—at least partly—by leaching. The dissolution mechanisms may therefore depend on the long-range order of the materials, leading to an absence of mechanistic continuum between minerals and glasses. Moreover, the mechanism may change according to the pH domain.

Building upon the work of Pérez et al.[1], the alteration mechanisms of amorphous and crystalline oligoclase with composition close to the albite end member were here investigated at 90 °C in acidic solutions (pH 1.5 and 3) saturated with respect to amorphous silica enriched in $H_4{}^{29}SiO_4$(aq) (see section 5, Methods). The main difference with previous work[1] is that the present study does not focus on the measurement of dissolution rates through ICP–AES analyses and surface-topography measurements, but rather on the dissolution mechanisms occurring at the molecular scale, unraveled using isotopic analyses and nm-scale analyses of the reacted solids (ToF-SIMS and FIB–TEM). Furthermore, additional specific experiments were conducted to compare the reactivity of amorphous and crystalline oligoclase at pH 3, which is close to the supposed threshold for the passivation of crystalline feldspars (around pH 2.5[49]). As Gin et al.[50] confirmed the passivating role of the altered layer using ^{18}O-labeled water and rejected the CIDR mechanism for a reference 6 oxide borosilicate glass called ISG[51] by showing that ^{29}Si is not incorporated in passivating gels formed under silica-saturated conditions, the diffusivity and the exchange rate of Si with the growing altered layer were investigated through ^{29}Si labeling, providing direct information on the corrosion mechanism at acidic conditions. In addition, Valle et al.[21] and Bouakkaz et al.[52] demonstrated that secondary phases such as phyllosilicates formed at equilibrium with the bulk solution and that ^{29}Si from solution could also incorporate in porous and low-passivating gel layer formed far from silica saturation. In those cases, the isotopic signature of the gel layer was intermediate between the glass and the solution, leading Gin et al. to conclude that a hydrolysis–condensation reaction mechanism controls the formation of passivating gel layers on silicate glass[48]

In the following, we test the hypothesis of the mechanistic continuum proposed in the conclusion of Pérez et al. between the reactivity of amorphous and crystalline glasses and the effect of long-range atomic order on the dissolution mechanisms of silicates. We show below that our results are compatible with the existence of a mechanistic continuum between glass and mineral dissolution, i.e., depending on the reaction conditions, both the CIDR and the leaching mechanisms may (sequentially) apply.

RESULTS

Initial parameters

Two sets of experiments were conducted in order to study the dissolution of oligoclase samples, one amorphous, one crystalline, for two different durations (12 and 33 days) at two different pH (1.5 and 3, see "Methods"). For a better understanding, the glass sample is labeled with a capital 'G' and the crystalline sample with a capital 'C'. The number that follows the letters refers to the pH of the solution at which the experiment was conducted. So G1 refers to the glass sample dissolved at pH 1.5 and G3 at pH 3. The same holds for crystalline samples C1 and C3. The last number refers to the series (e.g., C1–1 refers to the C1 sample altered 12 days and C1–2, the C1 sample altered 33 days). The starting parameters are listed in Table 1. All experiments conducted with crystalline samples were performed at far-from-equilibrium conditions with respect to albite ($\Delta G < -70$ and -35 kJ.mol^{-1} for experiments

Table 1. Experimental parameters used for oligoclase dissolution.

Sample	Surface (mm²)			pH initial	Exp. time (d)
	Top surface area	Total surface area	Uncertainty		
pH 1.5					
C1–1	16.8	33	±36%	1.4	12
C1–2	14.1	33	±21%	1.5	33
G1–1	9.0	54	±24%	1.4	12
G1–2	13.7	54	±20%	1.5	33
pH 3					
C3–1	19.1	34	±24%	2.9	12
C3–2	22.4	33	±18%	2.9	33
G3–1*	8.6	30	±33%	2.9	12
G3–2	5.4	38	±26%	2.9	33

*Note that the experiment conducted with the glass sample at pH 3, which lasted around 12 days, was found to be contaminated with trace concentrations of Mg and Fe resulting from imperfect cleaning of the reactor (0.62 ppm of Mg and 0.082 ppm of Fe). Thermodynamic calculations demonstrated that this contamination did not affect the dissolution of oligoclase sample.
The first column refers to the sample. The surface area exposed to the solution is then reported, with the Top Surface area corresponding to the upper surface, the Total Surface area corresponding to the surface area of the Top Surface plus the lateral surfaces and last, the uncertainty of the surface area measurement. The initial pH measured at 25 °C and the total duration of the experiment are listed in the subsequent columns.

conducted at pH 1.5 and 3, respectively, see Supplementary Tables 1 and 2).

Characterization of altered sample surfaces

A common trait of all characterized samples consists in (i) the lack of surface retreat that could have resulted from dissolution, as evidenced by vertical scanning interferometry (VSI) measurements and (ii) the formation of amorphous silica-rich surface layers (ASSLs). However, their morphology, thickness, texture, and chemical composition revealed by transmission electron microscopy (TEM) analyses realized on cross sections prepared by focused ion-beam (FIB) milling significantly differ from one sample to another (Figs. 1 and 2).

Crystalline oligoclase samples reacted at pH 1.5 and pH 3. The dissolution of crystalline samples is characterized by the formation of striations in the plane of the surface exposed to the solution (Fig. 1a and Supplementary Fig. 2). As can be seen in Fig. 1a and Fig. 1b, such striations result from the alternation of 30- to 44-nm-wide lamellae either enriched (Ca/Si = 0.024) or depleted (Ca/Si = 0.013) in Ca, which dissolved at specific rates, revealing a preferential alteration of the Ca-rich lamellae (this observation is consistent with the greater reactivity of Ca-rich vs. Na-rich feldspars, see e.g.,[53]). This heterogeneous dissolution is more pronounced at pH 1.5 (depth of one groove after 33 days ranging between 98 nm and 137 nm) than at pH 3 (depth <4 nm), so that the striations of the surface of C3–2 are hardly visible on scanning electron microscopy (SEM) images of the surface (Fig. 1b). Interestingly, most of the ASSL is located in-between the Na-rich lamellae revealed by dissolution at pH 1.5, ranging between 43 nm and 128 nm in thickness after 33 days (Fig. 1a). Conversely, the ASSL is much thinner (7 nm) and more homogeneously distributed at the surface of the sample reacted at pH 3 (Fig. 1b). Nanometer-sized pores are observed in the ASSL developed on the surface of C1–2 sample, appearing as dark spots in dark-field STEM images (Fig. 1a). The porosity is estimated to be ~12% by thresholding of dark-field STEM images[54]. In addition, high-resolution TEM images show that the interface between the altered layer and the pristine material is well delimited, with a sharp boundary between the crystalline and amorphous regions (Supplementary Fig. 3). The ASSL developed on C1–2 sample is depleted in Al and Na (Fig. 1a), as revealed by energy-dispersive X-ray (EDX) analyses—note however that the results of Na concentrations are poorly reliable due to the typical migration of alkali ions under the electron beam. The Al profile at the interface between the ASSL and oligoclase is quite sharp (Fig. 1a and Supplementary Fig. 4). Of note, ASSLs developed on samples reacted at pH 3 are too thin to be analyzed by EDX.

Oligoclase glass samples reacted at pH 1.5 and pH 3. As opposed to the ASSLs developed on the crystalline samples, the altered layers developed on the glass samples are continuous and cover the uncorroded glass homogeneously (Fig. 2a). The ASSLs are thicker on G1–2 (~120 nm) than on G3–2 (30–50 nm). In addition, altered layers are systematically thicker for glass samples compared with their crystalline equivalent at similar pH. Finally, EDX analyses performed on G1–2 (respectively G3–2) reveal that the depletion of Al is more gradual than for C1–2 (respectively C3–2), extending from a depth located between 50 nm and 110 nm from the sample surface (respectively between 25 nm and 50 nm).

ToF-SIMS analyses

ToF-SIMS analyses provide information regarding the alteration of the core material using the depth profiles of Na, Al, ^{28}Si, and ^{29}Si. Such profiles are shown under the form of $(X/^{28}Si)/(X/^{28}Si)_{substrate}$ ratios (hereafter referred to as X/Si ratios) in Fig. 3, where X = Na, Al. Because the ^{29}Si/^{28}Si ratio is quantitative (the ionization efficiency being the same for both isotopes), the corresponding ratio is not renormalized to its value in the parent materials. As emphasized in the previous section, the ASSLs are depleted in Na and Al, so that the Na/Si and Al/Si ratios are usually used as a proxy for the thickness of the altered layer.

A common feature of all profiles, regardless of the considered element, is that no sharp transition between the ASSL and the pristine sample is observed. In addition, the Al/Si profiles at the very surface (depth = 0 nm) never reach 0 for the crystalline samples, which is at odds with the TEM results, at least for those reacted at pH 1.5 (Fig. 1a). Those results stem from the fact that the profiles are artificially broadened due to the poor lateral resolution of the ion-beam imprint and the roughness of the altered surface, so that part of the parent substrate is analyzed right from the first cycle of Tof-SIMS measurements, together with the ASSL. To carefully address this problem, below, we first describe the raw depth profiles, prior to reporting the results of the profile deconvolution. Overall, the depth profiles vary as a function of the pH conditions, the long-range order of the samples, and the nature of the considered element.

Crystalline oligoclase samples reacted at pH 1.5 and pH 3. Consistent with the TEM results, the ASSLs developed on C1 samples are thicker than those developed on C3 samples, regardless of the element considered to estimate their thickness. In addition, the profiles extend over larger distances for samples reacted over longer durations (quantitative estimates based on the deconvolution of the profiles are discussed in section 2.3.3).

Regarding samples reacted at pH 1.5, the depth over which the X/^{28}Si ratios ($d_{X/28Si}$) vary until reaching a plateau observes the following trend, regardless of the duration of the experiment: $d_{29Si/28Si} \sim d_{Al/28Si} > d_{Na/28Si}$. Conversely, the samples reacted at pH 3 exhibit the following trend: $d_{29Si/28Si} \sim d_{Al/28Si} \sim d_{Na/28Si}$, for both durations (Fig. 3). The ^{29}Si/^{28}Si ratio is higher in the altered layer than in the pristine material and decreases until reaching

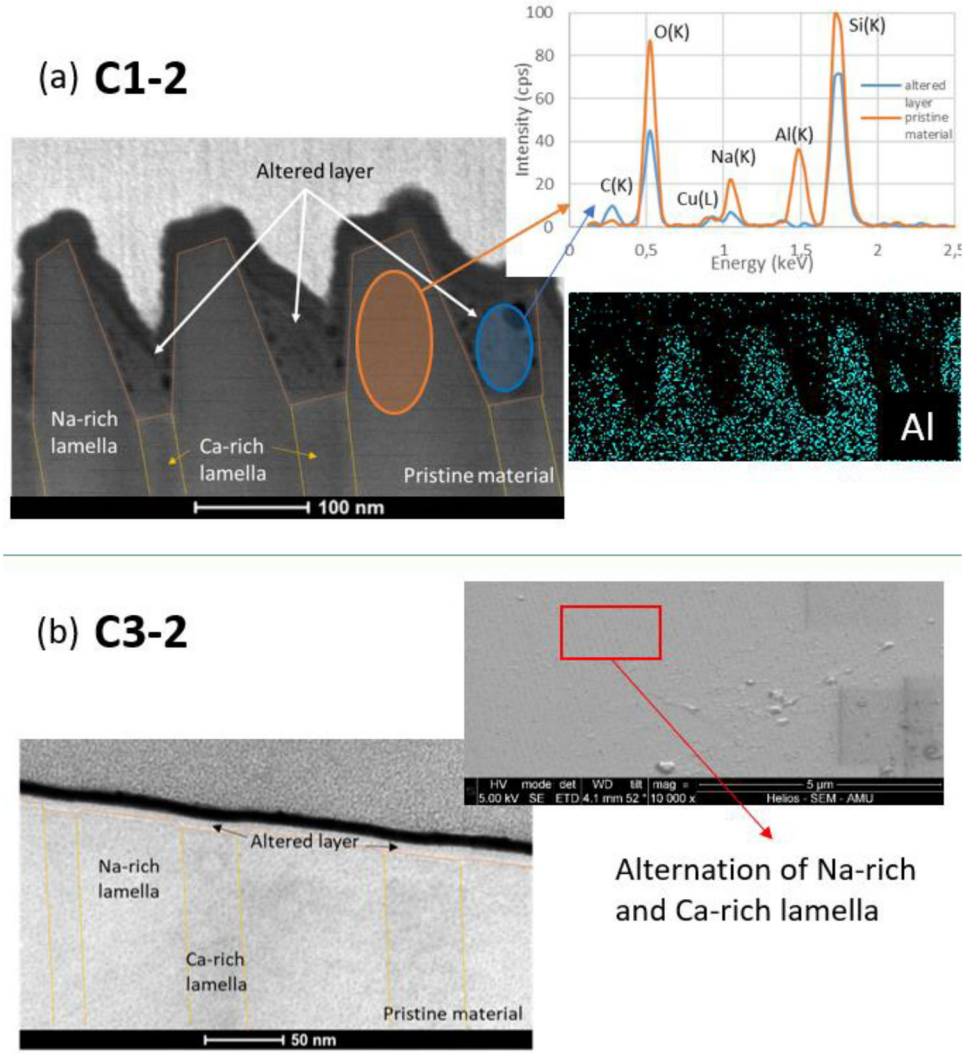

Fig. 1 Characterization by FIB–TEM of the surface of the crystal samples after 33 days of alteration. The composition of the altered layer and the pristine material was obtained by STEM-EDX. **a** TEM dark-field image of the interface between the crystalline oligoclase and the altered layer at pH 1.5 after 33 days of alteration (sample C1–2). A STEM-EDX map at the Al K edge is also shown, as well as EDX spectra collected on the crystalline sample and the altered layer. **b** TEM image of the crystalline sample altered at pH 3 after 33 of alteration (sample C3–2) shown in cross section. The striation of the surface resulting from the difference of reactivity between Ca-rich and Na-rich lamellae can be seen on the top view of the sample imaged by SEM (sample tilted at 52°).

the natural abundance around 0.05 (Fig. 3c, f). Similarly to the other ratios, the $^{29}Si/^{28}Si$ ratio decreases over shorter distances at pH 3.

Oligoclase glass samples reacted at pH 1.5 and pH 3. Similarly to the crystalline samples, the ASSLs developed on G1 samples are thicker than those developed on G3 samples, regardless of the element considered to estimate their thickness. For the same pH, the ASSLs developed on glass samples are also thicker than those developed on crystalline samples. The depth over which the $X/^{28}Si$ ratios vary until reaching a plateau displays the following trend, regardless of the duration of the experiment or pH: $d_{29Si/28Si} \sim d_{Al/28Si} < d_{Na/28Si}$. Conversely, the samples reacted at pH 3 exhibit the following trend: $d_{29Si/28Si} \sim d_{Al/28Si} \sim d_{Na/28Si}$, for both durations (Fig. 3).

Deconvolution of the Tof-SIMS depth profiles. As mentioned above, the $X/^{28}Si$ profiles appear to be broadened due to the lateral ion-beam imprint (and the patterning of the surface for altered crystalline samples). For each sample, the artificial broadening of the signal measured by ToF-SIMS is corrected by using a convolution function that is supposed to reflect the combined effects of the instrument resolution and surface roughness (see Supplementary Note 3). The outputs of the procedures are referred to as the "numerical profiles" and are supposed to be close to the actual depth profile of $^{29}Si/^{28}Si$. The fitting procedure consists in optimizing the parameters of the Gaussian function accounting for the broadening of the profiles, so that the difference between the measured profiles provided by ToF-SIMS and the convolution of the known actual Al/Si profiles (obtained from FIB–TEM measurements) with the Gaussian function (i.e., the "convoluted" profiles), is minimized (see Supplementary Note 3). The same Gaussian function is then applied to the $^{29}Si/^{28}Si$ profile measured by ToF-SIMS to estimate the corresponding $^{29}Si/^{28}Si$ "numerical profiles".

The sample G1–1 is chosen below as an example for the whole process. As can be seen in Fig. 4a, the fit between the $^{29}Si/^{28}Si$ convoluted profiles and the measured ToF-SIMS profile is satisfactory. The difference between each convolution and the measured profile is calculated using the root mean square (RMS) over a depth twice the size of the altered layer. The highest

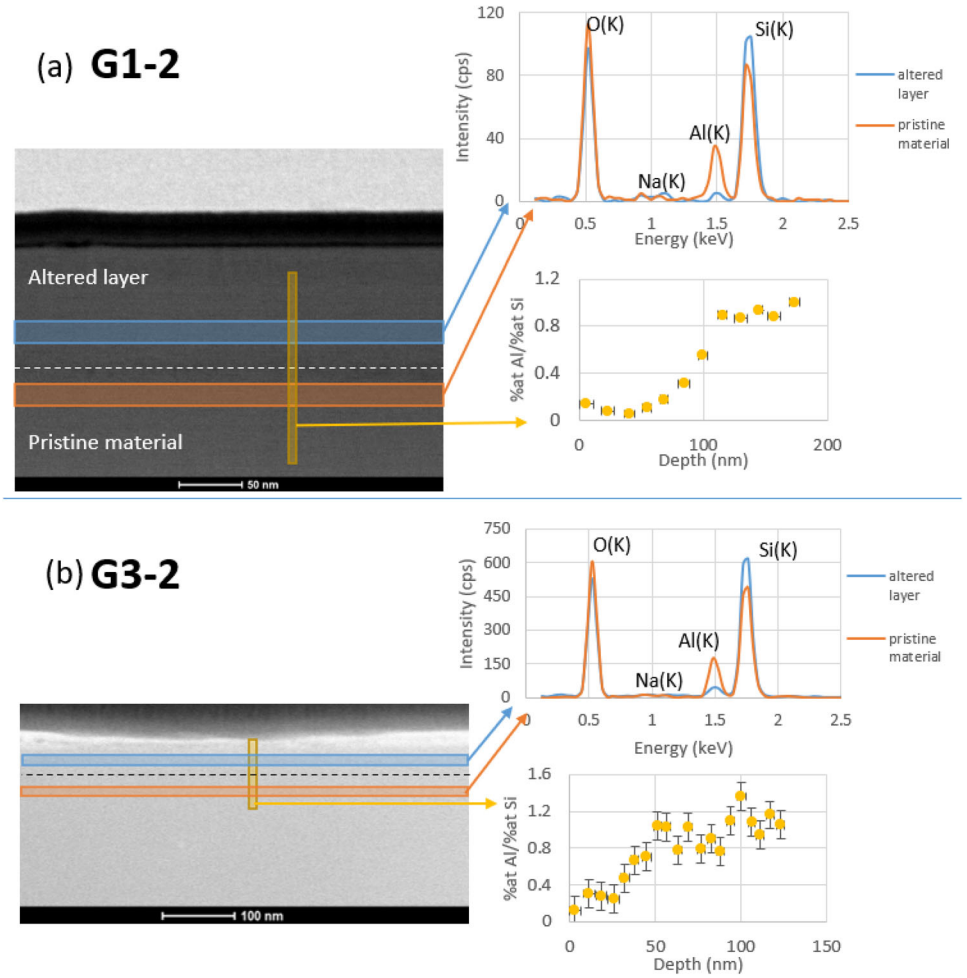

Fig. 2 Characterization by FIB–TEM of the surface of the glass samples after 33 days of alteration. The composition of the altered layer and the pristine material was obtained by STEM-EDX. **a** TEM dark-field image of the interface between the amorphous oligoclase and the altered layer at pH 1.5 after 33 days of alteration (sample G1–2). EDX spectra collected on the glass sample and on the altered layer are shown. The dashed line corresponds to the interface between altered layer and pristine material. **b** TEM image of the amorphous sample altered at pH 3 after 33 days of alteration (sample G3–2) shown in cross section. The interface between altered layer and pristine material represented by the dashed line was revealed using EDX analyses.

relative RMS is 11% for G3–1, while the lowest is 4% for G3–2. An average relative RMS, representative of the experiment, is around 5–7% for C1–1, C1–2, C3–1, C3–2, and G1–1. An exception is observed for G1–2, which has a relative RMS between 19% and 41%.

The best 10 numerical profiles corresponding to those with the lowest RMS are illustrated in Fig. 4b for G1–1. All profiles are located inside a narrow envelop that is suggested to reflect the actual $^{29}Si/^{28}Si$ profile. Knowing the $^{29}Si/^{28}Si$ ratio in the solution and in the pristine glass (which is the natural abundance), the contribution of the solution to the ASSL can be retrieved all along the depth profile.

Furthermore, we note that the average contribution of those profiles to the composition of the altered layer is almost identical for all profiles (15% ± 1%). In other words, the solution contributed to 15% of the Si content of the altered layer.

The average contribution for all samples is shown in Fig. 4c. Except for sample G3–2, the contribution of the fluid is systematically greater in strongly acidic condition, which is consistent with the observation of the raw $^{29}Si/^{28}Si$ profiles depicted in Fig. 3. The contribution of the fluid is larger for the crystal at pH 1.5 than for the glass at a similar pH and vice versa at pH 3. No systematic temporal trend is observed.

Regarding the thickness of the ASSL estimated from Al/^{28}Si profiles, the following observations can be drawn (Fig. 4d): (i) the layers grow with time, except for C3, where the layer seems to have a steady-state thickness, (ii) as suggested by the raw Tof-SIMS profiles, for a given pH, the layers are thicker on glass than on crystalline oligoclase, and (iii) the layers are thicker at pH 1.5 than at pH 3.

ASSL thickness estimated from solution analyses

In addition to the characterization of the reacted solids, the solutions were analyzed regularly by inductively coupled plasma–atomic emission spectroscopy (ICP–AES) in order to monitor the oligoclase dissolution. As expected, the Si and Na concentrations remain constant, within uncertainties (±3%), because of the elevated background level of those elements (see Methods). Based on the release of Al in solution, the thickness of the altered layer is calculated (see Methods) and compared with the thickness provided by ToF-SIMS/FIB–TEM characterizations. The thickness calculated using ICP–AES is 10 times greater than that estimated using ToF-SIMS measurements for oligoclase glass, and 30–70 times greater for the crystalline oligoclase (see Supplementary Tables 1 and 2 for ICP–AES data and Supplementary Tables 4 and 5 for ICP-MS data). A careful investigation of the

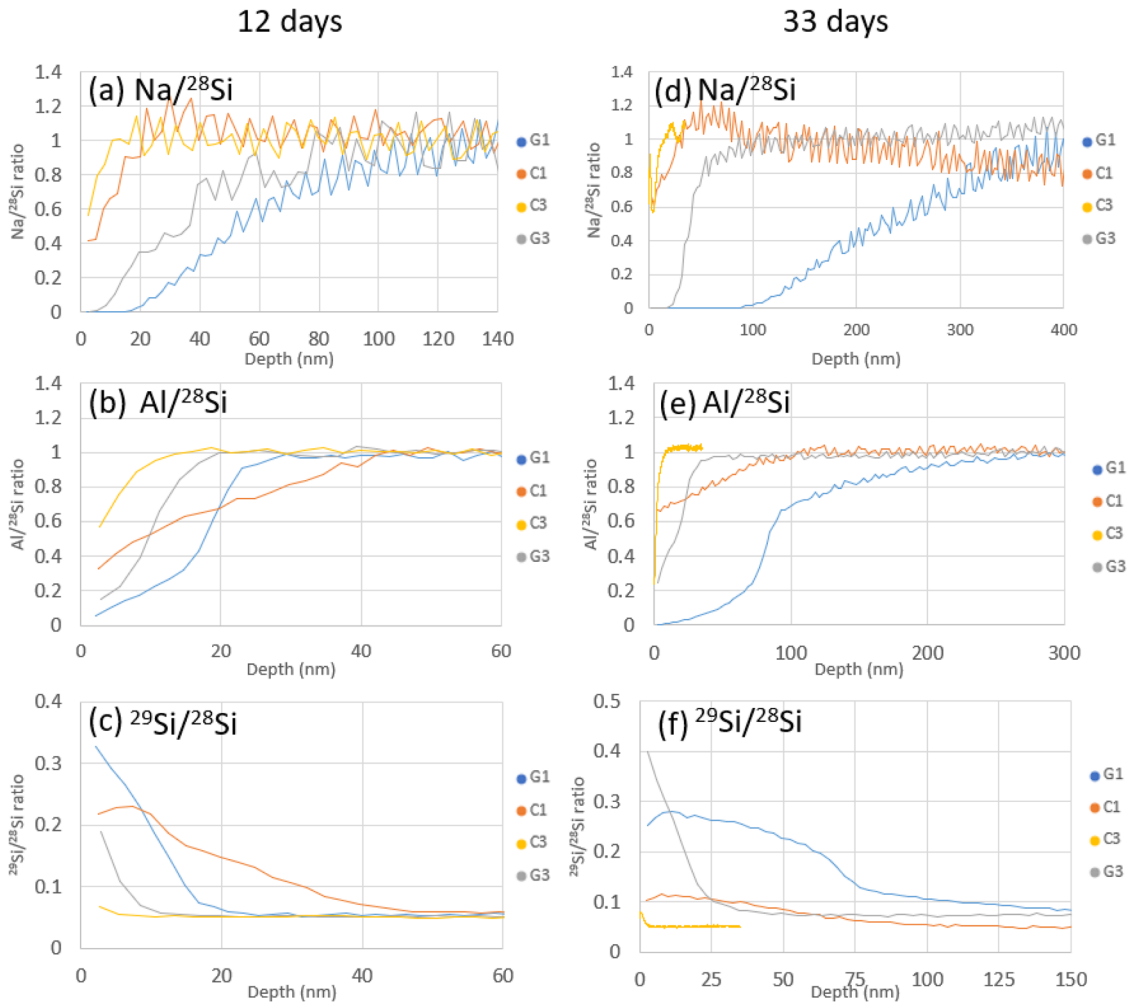

Fig. 3 Depth profiles of Al, Na, and 29Si collected with ToF-SIMS after 12 days and 33 days of alteration. Curves were normalized to the amount of 28Si. The blue curves, G1, refer to the profiles collected on the glass samples altered at pH 1.5. The orange curves, C1, refer to the mineral samples altered at pH 1.5. The gray curves, G3, refer to the glass samples altered at pH 3. The yellow curves, C3, refer to the mineral samples altered at pH 3.

reacted samples reveals several features that might contribute to such discrepancies (see Fig. 5 and section 3.1):

(i) First, an ~40- to 100-µm-wide gap is observed between the epoxy resin and the oligoclase samples for all experiments (Fig. 5a–c). Observations performed on unreacted spare samples show that this detachment is present for all samples prepared on the same day. It can therefore be reasonably assumed that the lateral faces of each sample, which were not polished before the reaction, contributed to the flux of Al released to the solution.
(ii) Bubbles of ~10–150 µm in diameter resulting from the manufacturing of the glass samples are found to outcrop at the surface of all oligoclase glass samples (Fig. 5a–c).
(iii) Finally, regarding the crystalline oligoclase samples, deep trenches are observed on reacted surfaces, as well as K-feldspar veins, revealing the perthitic nature of the crystals (Fig. 5d, e). The accurate depth of those trenches is out of reach of VSI measurements.

Overall, the surface area in contact with the solution was recalculated after measuring the surface of the lateral faces to consider their contribution in the alteration process. The corresponding altered-layer thicknesses estimated based on ICP–AES data are significantly lowered (Fig. 6), reducing the gap between the thickness estimated from solution analyses ($h_{solution}$) and those estimated from ToF-SIMS measurements ($h_{ToF\text{-}SIMS}$). Whereas the $h_{solution}/h_{ToF\text{-}SIMS}$ ratios of three of the four reacted glass samples are within a 2-fold factor, the $h_{solution}/h_{ToF\text{-}SIMS}$ ratios still exceed one order of magnitude for most of the reacted crystalline samples.

DISCUSSION

Discrepancies between solid and fluid characterizations: a possible evidence for the development of supplementary reactive surface area for crystalline samples

When the thickness of altered oligoclase glass estimated from solution analyses is compared with that estimated from solid characterizations (ToF-SIMS and FIB–TEM analyses), a ≥twofold factor between each estimation is found (Fig. 6). This factor is calculated after accounting for all the adjacent surfaces. Because of the amorphous structure of the glass, the dissolution of such samples is isotropic, so that the lateral faces should dissolve at the same rate as the top face and should not increase the total dissolution rate. Considering however the extra surface area resulting from (i) the numerous bubbles outcropping at the surface (Fig. 6a) and (ii) the fact that the lateral faces were not polished, this twofold factor between the Tof-SIMS and the ICP–AES estimates could be reasonably considered as negligible.

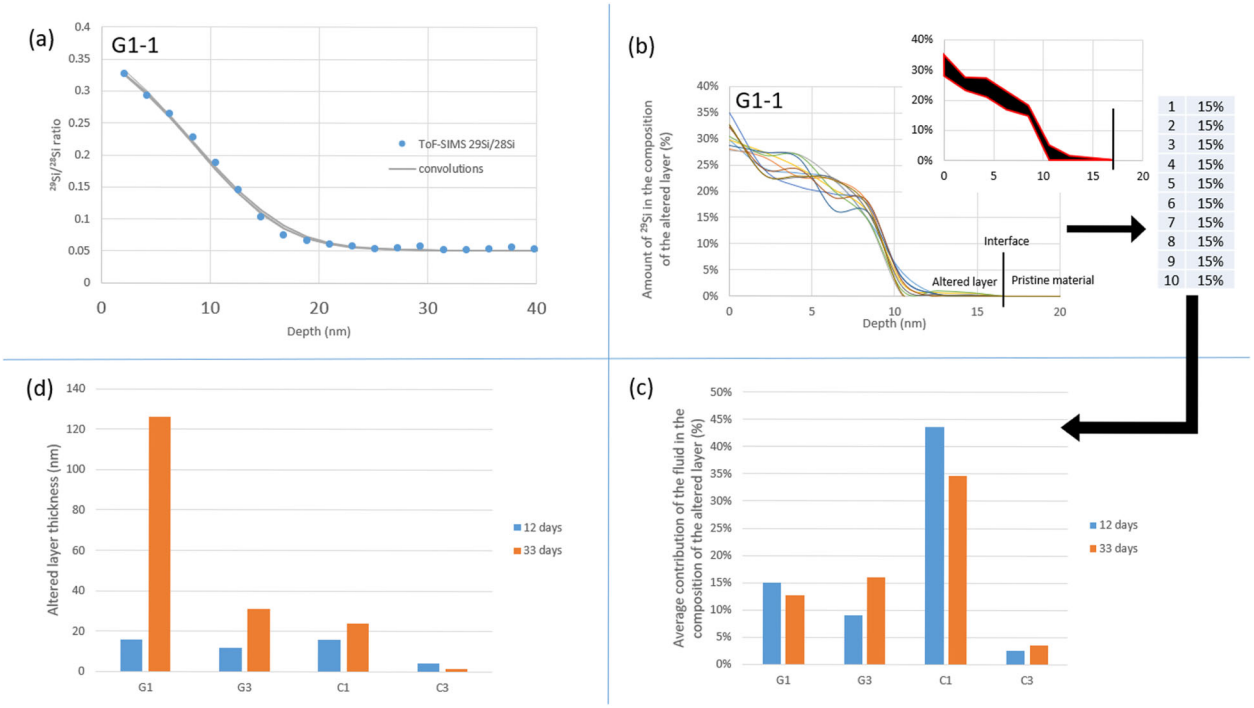

Fig. 4 Results from the deconvolution of the ToF-SIMS depth profiles. a Comparison between the ToF-SIMS depth profile and the numerical profiles of the amorphous oligoclase altered at pH 1.5 after 12 days (sample G1–1). **b** Plots depicting the best 10 numerical profiles of G1–1, the envelop created by those profiles and the average contribution of the solution to the composition of the altered layer for each profile. **c** Representation of the average contribution of the fluid in the composition of the altered layer for each sample. **d** Representation of the altered-layer thickness for each sample based on Al/^{28}Si ToF-SIMS profiles.

Interestingly, such discrepancies are similar to those reported by Fournier et al. [55] when comparing the reactivity of polished glass monoliths to that of glass powders, which is typical of the additional contribution of surface roughness.

Regarding the crystalline samples, the ratios between altered thickness estimates from fluid data to solid characterizations range from 16 for C3–1 to 60 for C1–2. The top face was determined to be a (001) face, which represents the fastest-dissolving faces among the (001), (010), and (10-1) faces studied by Pérez et al.[1]. Due to the crystalline structure of the sample, dissolution is expected to be anisotropic, and the rate of the unpolished lateral faces may be either greater or lower than that of the top (001) face, which may partly explain the large discrepancies between estimates derived from fluid vs. solid characterizations. However, even the thorough work of Pollet-Villard et al. [56] dedicated to the dissolution anisotropy of K-feldspar did not evidence discrepancies as large as ~ two orders of magnitude between two dissolving faces. This observation leads us to suggest that intracrystalline reaction might have occurred as well, partly due to the perthitic nature of the sample we used, as testified from the deep trenches observed at the surface of the sample (Fig. 5d, e). Lee et al.[57] demonstrated that the microtexture of feldspars and especially, the boundaries between the feldspar matrix and exsolution lamellae, represents hotspots of reactivity. The dissolution rate at the interface between those two phases is greater, and since this interface gets deeper into the core material, the dissolution proceeds unhindered along their interface. In other words, those interfaces may represent additional surface area where dissolution occurred. Moreover, an alternation of Ca-rich and Na-rich lamellae was observed, leading to the preferential dissolution of Ca-rich lamellae. The edges and corners of this structure may contribute to increase the dissolution rate. Finally, Worden et al.[58] demonstrated that the turbidity of feldspars is correlated with the presence of micropores. The coarsening of the perthites on the surface involves the outcrop of those micropores. The border between boundaries gets thinner and diffusive intracrystalline channels may develop, increasing the exchange surface with the solution. Once the dissolution front crosses those micropores and channels, intracrystalline reaction takes place and increases the dissolution rate.

In summary, while the results obtained to quantify the dissolution rate of oligoclase glass can be reasonably well explained by the contribution of unpolished lateral faces, it is more difficult to draw a similar conclusion for the crystalline samples. The discrepancies between the estimations based either on fluid data or solid characterizations may be ascribed to an additional intracrystalline reactivity fostered by the perthitic nature of the crystalline samples.

Dissolution mechanisms inferred from solid characterizations

FIB–TEM characterizations and elemental depth profile suggest that the dissolution mechanisms depend on the long-range order of the materials. Figures 1 and 2 summarize FIB–TEM characterizations for the samples altered over 33 days. When these results are coupled with Na and Al depth profiles collected using ToF-SIMS (Fig. 3), a first approach to the alteration mechanism can be proposed.

Regarding oligoclase glass, FIB–TEM characterizations reveal that the Al/Si ratio exhibits a gradual transition from the pristine sample to the ASSL, spreading over 50 nm at pH 1.5 and 25 nm at pH 3 (Fig. 2a, b). Such a gradual transition can also be observed from ToF-SIMS characterizations (Fig. 3), although one must keep in mind that such profiles are more sensitive than FIB–TEM measurements to broadening. A more robust observation stems from the comparison of the profiles as a function of the considered element: the depletion depth is element-dependent. While Na is depleted to a depth of 500 nm in the glass sample at pH 1.5 after 33 days, the Al depletion front reaches barely 300 nm.

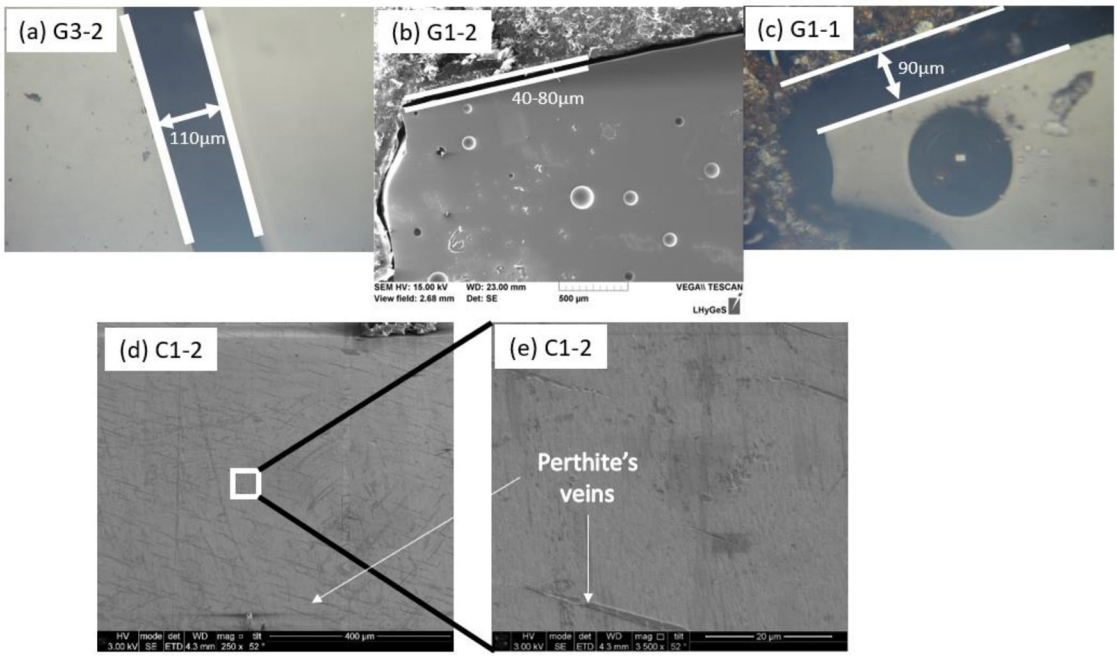

Fig. 5 Optical microscope and SEM images of the surface of the altered samples. a–c Pictures showing the retraction of the resin and the gap of several tens of micrometers created between the sample and the resin. Those microscopy images are from amorphous oligoclase altered at pH 3 for 33 days ((**a**) sample G3–2) and at pH 1.5 for 12 days ((**c**) sample G1–1) and 33 days ((**b**) sample G1–2). A similar retraction is observed on crystalline oligoclase. **d, e** Pictures showing the presence of K-feldspar veins on the surface of crystalline oligoclase at pH 1.5 after 33 days of alteration (sample C1–2) with a magnification of (**d**) 250x and (**e**) 3500x. The K-feldspar veins are labeled as perthite's veins as they are a consequence of the perthitic nature of the material.

A similar observation can be made for all amorphous samples at pH 1.5 and 3, after 12 days or 33 days. Based on those observations, a leaching mechanism is likely to occur during the dissolution of oligoclase glass. In addition, while under strongly acidic conditions, the dissolution rate does not decrease with time, a significant decrease in the dissolution rate is observed at pH 3 between 12 and 33 days (Fig. 4d), which is consistent with the pH-dependent passivating properties of ASSLs formed on silicate glass[28,59]. Note that in the following, we refer to "passivation" when a decline of the transport properties of the ASSLs is observed or suspected. We do not distinguish between a scenario where the transport of aqueous species through the layer became impossible (thereby corresponding to "passivating layers", strictly speaking) or only dramatically decreased.

Regarding crystalline oligoclase, STEM-EDX characterizations of the C1–2 sample show that the Al/Si profile is very sharp at the interface between the altered layer and the pristine crystal (note that this step-like profile supports the model used in Supplementary Note 3 to deconvolute the ToF-SIMS profiles). Furthermore, the structural interface is sharp and well delimited, extending over a few nanometers only. Finally, the alternation of Ca-rich and Na-rich lamellae translates into a difference of reactivity of each domain. A similar observation prompted Wild et al[49] to reject a leaching mechanism for the dissolution of labradorite at pH 1.5 and 3. Instead, all these observations suggest that crystalline oligoclase dissolves following the CIDR mechanism at pH 1.5[37–39]. This hypothesis is further supported by the porosity of the altered layer: the difference between the molar volumes of amorphous SiO_2 and oligoclase is consistent with the porosity estimated from TEM images. At pH 3, we can observe a slight preferential dissolution of Ca-rich lamellae, resulting in a similar (though greatly attenuated) grooved interface, consistent with the CIDR mechanism. However, the altered layer is only a few nanometers in thickness, and does not evolve between 12 days and 33 days (Fig. 4d). Consistent with the observation of Wild et al.[49] for labradorite, we conclude that the crystalline oligoclase is passivated at pH >3. The limited thickness of the ASSL prevented us from getting detailed information on its chemical composition, so that detailed dissolution mechanisms remain out of reach. However, we suggest that the difference in the evolution of altered-layer thickness between the crystals at pH 1.5 and pH 3 can be explained by a competition between the dissolution rate of the oligoclase and the densification of the ASSL, as proposed by Daval et al.[45] for wollastonite. Under strongly acidic conditions, the densification kinetics may be slower than the dissolution rate, resulting in nonpassivating surface layers, as opposed to those developed under less-acidic pH conditions.

In summary, the combination of FIB–TEM characterizations with depth profiles measured by ToF-SIMS suggests that oligoclase glass dissolution may follow a leaching mechanism, whereas oligoclase crystal dissolution observes a CIDR mechanism.

Dissolution mechanisms inferred from $^{29}Si/^{28}Si$: a new perspective on the dissolution process for crystalline samples?. As mentioned previously, we used ^{29}Si as a proxy for the alteration mechanism. If the altered layer is a relic structure of the pristine material resulting from preferential leaching, the isotopic composition of the leached layer should be the same as that of the pristine material. Conversely, if the layer is formed following a CIDR mechanism, it should record the isotopic composition of the fluid[22,50]. This protocol was previously successfully applied on borosilicate alteration[50] vs. Si–K–Ca glass alteration[60], with contrasted results regarding the isotopic signature of the ASSLs, and therefore, their mechanisms of formation. Figure 4c summarizes the contribution of the solution in the composition of the altered layer.

As a confirmation of the previous conclusions (see section 3.2.1), we note a negligible incorporation of ^{29}Si in the layer of glass samples reacted at pH 1.5 and pH 3 (contribution of the fluid ≤16%). Thus, most of the Si is inherited from the glass samples. The altered layers are essentially relics of the pristine glass, which therefore mainly dissolves by releasing first Na and to a lesser

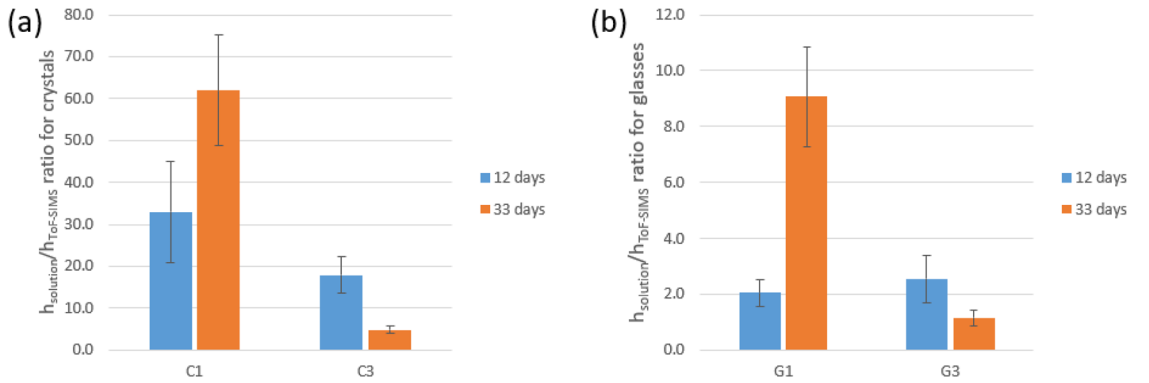

Fig. 6 Representation of $h_{solution}/h_{ToF\text{-}SIMS}$ ratio for the various samples. Those samples are (**a**) crystalline oligoclase altered at pH 1.5 (labeled as C1) and at pH 3 (labeled as C3) and (**b**) amorphous oligoclase altered at pH 1.5 (labeled as G1) and at pH 3 (labeled as G3). Uncertainties are detailed in Supplementary Note 3.

extent Al without getting the silica matrix dissolved (depletion front of Al at 30 nm for G1–1 or 20 nm for G3–1 vs. a depletion front of Na at 140 nm for G1–1 or 80 nm for G3–1). The slight incorporation of ^{29}Si from the fluid may indicate a minor contribution of precipitated silica in the layers.

The results obtained on crystalline samples are more intriguing: the $^{29}Si/^{28}Si$ ratios measured with ToF-SIMS indicate that the contribution of the fluid only amounts to 35–45% for the ASSLs developed on crystalline samples altered at pH 1.5. According to the FIB–TEM observations, a much higher value (close to 100%) reflecting the CIDR mechanism was expected. Therefore, those results suggest that the CIDR mechanism cannot fully explain the alteration process of the crystalline samples. Two scenarios may be envisioned to solve this paradox. Both are based on a putative gradual modification of the transport properties of the altered layer with time (this assertion is supported by the nonlinear growth of the altered layer with time, cf. Fig. 4d):

(i) If the ASSL transport properties decreased, the pristine material became increasingly isolated from the ^{29}Si-enriched bulk fluid. Still, at such low pH, the oligoclase crystal remained undersaturated, and kept dissolving, so that the $^{29}Si/^{28}Si$ ratio in the pore fluid of the ASSL gradually decreased, and the isotopic signature of the precipitated silica gradually approached that of the pristine crystal.

(ii) Alternatively, part of the silicon from the oligoclase crystals might have not been released in the aqueous phase prior to its incorporation into the ASSL. Daval et al.[61] proposed a similar mechanism for the dissolution of crystalline olivine, where the ASSL forms following the CIDR mechanism first, while subsequent structural rearrangement of the altered layer results in solid-state diffusion of dissolved species throughout the ASSL. Of note, this scenario would contradict the premise that all Si–O–Si bonds must be broken simultaneously in order to release a Si atom in the solution (as suggested by the CIDR model). It could then be possible that Si–O–Si bonds are sequentially broken to release separately O and Si atoms into the solution. As long as one bond is not broken, Si is attached to the silica matrix and does not dissolve forming, thus, a leached layer. The in situ reorganization of the altered layer after the release of Na and Al then becomes the source of the formation of the altered layer. This reorganization implies that Si can form new bonds with other Si to reform a silicate network. This mechanism is supported by Gin et al.,[48] who conducted a study on the mechanism of formation of altered layer on borosilicate glass. Despite the difference in the structure of the materials, the common point of both studied materials is their composition with and without Al-bearing materials. The effect of the presence of Al will be discussed in the following section.

Overall, both scenarios account for (i) the temporal decrease in the contribution of the fluid to the composition of the ASSL developed on C1 samples (Fig. 4c) and (ii) the (modest) decrease in the dissolution rate of crystalline oligoclase with time (Fig. 4d). Similar scenarios could be envisioned for C3 samples, where the alteration might have taken place early before the formation of a passivation layer on the surface (Fig. 4d), and the contribution of the fluid to the ASSL became negligible (Fig. 4c).

Structure and texture effects on the dissolution rate

Penetration of water in the material and the impact of Al on dissolution rates and mechanisms. The presence of Al in the network of silicate glasses and minerals increases locally the bond-breaking activation energy of Si–O–Si bonds[62–64]. The corresponding Si atoms are then harder to dissolve. As a matter of fact, Al-bearing glasses dissolve slower than Al-free glasses[48]. Pierce et al.[65] promoted the cleavage of Al–O as the rate-limiting step in Al-bearing glass dissolution. Conversely, the activation energy for dissolving Al–O bonds is much lower than that of Si–O bonds[64], leading to a preferential release of Al in the solution. Once Al is depleted, the silicate network is weakened and the hydrolysis of the siloxane is much faster. By studying the dissolution of albite, jadeite, and nepheline glasses, Hamilton et al.[66] demonstrated that the higher the Al/Si ratio is in the glass, the faster the dissolution is in acidic condition. Stone-Weiss et al.[67] explained this observation by the hydrolysis of the Si surrounding Al (and B), which decreases the network connectivity. Taken together, those observations suggest that small amounts of Al in the glass strengthen the silicate network, while a more important amount is in favor of the network dissolution. The boundary between the two regimes remains to be determined.

From this point, a striking difference between crystalline and amorphous oligoclase is the more open structure of the latter (cf. Fig. 15 in Pérez et al.[1]). Molecular dynamics simulations conducted in this previous study show that the structure of the glass is more open, with interstitial sites having a radius that exceeds 1.3 Å. Such dimensions are compatible with molecular water diffusion into the material[7]. As a consequence, the inward flux of water may contribute to Si–O–Al and Si–O–Na hydrolysis. Those channels not only explain the depletion depth of Al and Na elements observed in our experiments for glass samples, but also the difference between the evolution of the altered-layer thickness between 12 days and 33 days for glass and crystal samples. Indeed, because diffusion channels do not exist in the crystalline oligoclase, its dissolution should be limited at the very surface. In order for this surface to be altered, Al depletion

is needed and only after this step, the breakdown of the silicate network can occur. But since the altered Si-rich layer condenses on the surface, the transport properties of this layer decrease, resulting in a decrease of the alteration rate. Conversely, the more open structure of the glass results in an alteration at the surface, but also within the glass. The deeper depletion of Al in the material implies a faster alteration of the silicate network. Because the reaction rate between the pristine material and the bulk solution remains high, the altered layer cannot densify or reorganize itself quickly enough to affect the dissolution rate, explaining its high value and thus, the dramatic increase in the thickness of the altered layer of G1 samples after 33 days. Such a reasoning would be consistent with the observation of Hamilton et al.[68] regarding the rate-limiting step of glass vs. crystalline albite dissolution.

Finally, Yang et al.[69] modeled the effect of Al/Si ordering on the development of interfacial layers on dissolved feldspars. They demonstrated that, in a disordered structure, the diffusivity of aqueous species in the material is limited by the hydrolysis rate of Si–O–Al bonds. The disordering of Al atoms that are gradually released to the solution may result in the development of channels within the material. On the contrary, in an ordered structure, the diffusivity of aqueous species is limited by both the hydrolysis rate of Si–O–Si and Si–O–Al bonds. Those observations support the fast dissolution of oligoclase glass at pH 1.5 and the slower dissolution of (ordered or disordered) oligoclase crystal in Fig. 4d.

A pH threshold for the passivating properties of ASSLs developed on crystalline samples. In a recent study, Daval et al.[45] reported that the passivating properties of ASSLs developed on various faces of a Ca-rich pyroxene (wollastonite) are negatively correlated with their absolute dissolution rates (i.e., the dissolution rates of ASSL-free faces). They proposed that the passivating properties of ASSLs result from a competition between the hydrolysis rate of the mineral and the densification rate of the ASSL. As a consequence, they speculated that any parameter favoring the densification of the layer at the expense of the hydrolysis of the mineral would result in a decrease of the transport properties of the ASSLs. Our results are consistent with this assumption: the hydrolysis rate of silicates is known to increase when pH decreases[70], whereas the condensation rate of silica is slower in acidic solutions[71]. As a consequence, one could expect that the reaction becomes transport-limited for layers developed at mildly acidic pH. Our results are also consistent with Wild et al.[49], who determined experimentally a pH threshold of 2.5, above which ASSLs become passivating for labradorite feldspar.

Discussion summary

Whether or not the mechanisms of silicate dissolution depend on its long-range order has long remained an open question. By comparing the reactivity of crystalline and amorphous oligoclase at pH 1.5 and 3, the following conclusions can be drawn:

(i) Regarding crystals, the estimated evolution of the thickness of surface layers with time suggests that the transport properties of surface layers decrease with pH. Whereas oligoclase dissolution rate is moderately impacted by the surface layers developed at pH 1.5, the oligoclase surface is passivated at pH 3.

(ii) Regarding crystals, FIB–TEM characterizations first suggested that the surface layers are formed following a coupled interfacial dissolution–reprecipitation (CIDR) mechanism (particularly evident at pH 1.5). However, Tof-SIMS measurements revealed that incorporation of ^{29}Si from the solution is only modest at pH 1.5 (between 35% and 45%) and insignificant at pH 3 (<5%), challenging the CIDR mechanism (which should correspond to a fluid contribution close to 100%, as noticed by Gin et al.[48]). We suggest that the evolution of the transport properties of the surface layers with time gradually isolates the oligoclase surface from the bulk fluid, so that the growth of the surface layers continues either without a full depolymerization of the silicate framework (solid-state diffusion), or through the uptake of SiO_2(aq) from the nanopores that is increasingly enriched in Si provided by the substrate.

(iii) Conversely, both FIB–TEM characterizations and Tof-SIMS measurements converge toward the same conclusion that proton diffusion inside the oligoclase glass structure could have contributed to the preferential leaching of Na and (to some extent) Al cations. The contribution of the CIDR mechanism is minor, but measurable (<20%). The existence of diffusion channels in the structure (as suggested by Pérez et al.[1]) favors the release of Al cations, resulting in the weakening of the silicate framework and an enhanced dissolution of the structure.

(iv) Finally, even if the understanding of the alteration mechanism is important in order to model the corrosion of such material over geological timescale, the key point is therefore the transport properties of altered layers. The ingress of protons is the driving force of hydrolysis and Si–O–Si or Si–O–Al bond cleavages. From this inward flow, a second outward flow starts with the depletion of material elements such as Na or Al. Those elements diffuse into the solution, leaving a weakened silicate network prone to dissolve. More experiments must be conducted in order to characterize the transport properties of those layers.

METHODS

Sample preparation

Oligoclase glass and mineral samples were prepared during the previous work of Pérez et al. [1]. According to this study, the chemical composition of the sample is $Na_{0.83}K_{0.02}Ca_{0.07}Al_{1.06}Si_{2.96}O_8$. The orientation of the oligoclase crystals was (001), as determined by electron backscatter diffraction (EBSD). Glass sample was prepared from melting the crystalline oligoclase at 1500 °C for 2 h and then 1650 °C for 2 h in a high-temperature furnace Carbolite HTF 1700 (see details in Pérez et al.[1]). As shown above, the cooling step resulted in the formation of bubbles within the oligoclase glass.

Oriented crystal and glass samples were embedded in epoxy resin, so that only the surface of interest was exposed at the surface of the resin (as emphasized above, this treatment was however unsuccessful, due to a strong retraction of the resin during its solidification). The samples were then polished through different steps of abrasion sequence, and subsequently divided into smaller pieces. The lateral sides of the samples that were not embedded in the resin were covered with room-temperature-vulcanizing (RTV) glue to prevent dissolution of unpolished parts of the samples. A small part (<1 mm^2, on average <9% of the top surface of the sample) of the polished surface of interest was protected as well with RTV glue spots to create a nonreacted reference surface.

Solution preparation

The experiments were conducted in solutions saturated with respect to amorphous silica (SiO_2(am)) to stabilize the Si-rich layer developed at the surface of the oligoclase during dissolution. The concentrations of Si were 175 ppm and 140 ppm (on average) for the 12-day and 33-day alteration experiments, respectively. The solution for the sample dissolution was enriched in ^{29}Si using amorphous silica $^{29}SiO_2$(am) powder (Cortecnet, 99.69% purity of ^{29}Si). To circumvent the sluggishness of SiO_2(am) dissolution, an alkali-fusion protocol was followed, where the $^{29}SiO_2$(am) powder was mixed with potassium hydroxide in an agate mortar ($mKOH/mSiO_2 = 10$). Mixed powder was placed in a zirconia crucible and introduced in a high-temperature oven (NABERTHERM). The temperature was increased to 300 °C in 2 hours and kept constant for 15 minutes while Ar gas was introduced. Then, it was increased again to 600 °C within an

hour and kept constant during 45 min before cooling down the oven. At 300 °C, Ar gas delivery was shut down and around 100 °C, the crucible was recovered from the furnace. The crucible was then immersed in a solution of HNO_3 0.1 N at 90 °C to dissolve the resulting Si-rich solid and stirred overnight at 90 °C. The analyses of dissolved Si concentration indicated that the yield of the fusion was approximately 60–70% of $^{29}SiO_2$ initially introduced. In a second stage, K^+ ions were removed from the solution, because of their potential effect on the transport properties of the altered layers[15]. We used a K^+/H^+ exchange resin column (AG50W–X12) to remove selectively potassium. Finally, in order to reach saturation with respect to amorphous silica at 90 °C, sodium metasilicate (Na_2SiO_3) was added to the solution, because of its large solubility and fast dissolution rate (see Supplementary Tables 4 and 5). The solution pH was then adjusted to either 1.5 or 3.0 (the given pH corresponds to the pH of the solution at 90 °C). It was measured at ambient temperature and then back-calculated at 90 °C using the thermodynamic code JChess, which accounts for the evolution of logK of the various species in solution with the temperature, using LiOH (Prolabo) and HNO_3 (distilled). Four 60-mL PFA Savillex® reactors were filled with ~35 ml of solution and placed in an oven at 90 °C. Each reactor contained either a glass or a crystalline sample placed on PTFE tripods inserted in the reactors. The solution was continuously stirred with magnetic bars.

After introducing the glass and crystalline samples in the reactors containing the prepared solution, the dissolution of the samples started in the oven at 90 °C. The dissolution was controlled by collecting a small amount of solution regularly. At the end of the experiment, both solution and sample provided information on oligoclase alteration.

Analyses

The dissolution process was controlled by collecting 1 ml of the solution every 5–7 days. The aqueous samples were then diluted 5x and analyzed with ICP–AES (Thermo ICAP 6000) for Na, Al, and Si, or 10x, and analyzed with inductively coupled plasma mass spectroscopy (ICP-MS) to determine the aqueous $^{29}Si/^{28}Si$ ratio of the solution. The measured concentrations were used to estimate the dissolution rate of the interface between the altered layer and the pristine substrate, which is referred to as the "internal interface" (see Wild et al. [49] for details), and provides indirect information on the growth rate of the altered layer. The depth profile of elements of interest was measured using time-of-flight secondary ion mass spectrometry (ToF-SIMS). This isotope-sensitive technique provides information about the mechanism of formation of the altered layer.

ICP–AES and ICP-MS analyses of aqueous solutions. Because of the small volume of solution, only a few intermediate samplings were performed to monitor the dissolution of oligoclase samples. At each sampling step, the amount of element *i* (mol) released into the fluid was calculated based on ICP–AES measurements following:

$$n_t^i = \frac{F_t \times [i]_t \times V_t}{M_i} + \sum_{l=1}^{t-1} \frac{[i]_l \times V_{ct} \times F_l}{M_i} \quad (2)$$

where n_t^i is the amount (mol) of element *i* at time *t*, F_t is the dilution factor of the aqueous sample collected at time *t*, $[i]_t$ and $[i]_l$ are the concentrations of element *i* at time *t* and *t* – Δ*t*, respectively, V_t and V_{ct} are the volumes of the solution in the reactor just before collection and the volume of the solution collected at time *t* respectively, and M_i is the molar mass of element *i*.

ICP-MS analyses were also performed to determine the aqueous $^{29}Si/^{28}Si$ ratio and estimate the incorporation of the ^{29}Si from the solution into the altered layer. However, being the uncertainties of the ICP-MS measurements around 3%, the difference between the initial and final ratios was not statistically significant. Consequently, the ICP-MS measurements were not accurate enough to estimate the thickness of the altered layers containing ^{29}Si.

Because sodium metasilicate was used to bring the solution at saturation with respect to SiO_2(am), the background concentrations of Na and Si were too high to provide any reliable information on the dissolution rate of oligoclase. Therefore, the dissolution rate at the internal interface (between the pristine material and the altered layer) was estimated based on Al concentration. Based on thermodynamic simulation and ICP–AES analyses, the solution remained undersaturated with respect to Al precipitates (diaspore, boehmite, and gibbsite) all over the duration of the experiment. After plotting the amount of Al as a function of time, we proceeded to a linear regression. The slope of the regression was then divided by the surface area of the corresponding sample to estimate the dissolution rate (r_{disso}, see Supplementary Fig. 1 and Supplementary Table 3)

$$r_{disso} = \frac{a_{lr}}{S_{total}} \quad (3)$$

where a_{lr} is the slope of the linear regression (mol.s^{-1}) and S_{total} is the total surface area—taking the lateral surfaces into account—(m^2) of the sample in contact with the solution.

Since the solution was saturated with amorphous SiO_2, no external surface retreat is expected at the interface between the solid and the solution. Topography data collected by vertical scanning interferometry (Zygo NewView 7300) confirmed this statement, as no difference of elevation between the masked reference surface and the reacted surface could be evidenced, consistent with Perez et al.[1]. The thickness of the altered layer estimated using fluid data (h_{ICP}) was therefore calculated as follows:

$$h_{ICP} = \frac{r_{disso} \times t_{exp} \times M_{olg}}{\rho_{olg}} \quad (4)$$

where t_{exp} is the duration of the experiment, M_{olg} is the molar mass of oligoclase (262.2 g.mol^{-1}), and ρ_{olg} is the density of oligoclase (2.62 g.cm^{-3}).

ToF-SIMS analyses of the reacted surface. The altered solid samples were analyzed by an IONTOF GmbH® TOF 5 spectrometer from TESCAN Analytics (France). The external surface was abraded on an area of 200 × 200 µm^2 for an analyzed area of 50 × 50 µm^2. The ToF-SIMS operated as cycles of abrasion and analysis. After each cycle, the surface charge was neutralized by a low-energy electron beam (<20 eV) in order to prepare the area for the next cycle. The depth of the crater (h_{crater}) created by ion milling after a given number of abrasion cycles (N_{cycles}) was measured using 3D profilometer. The depth associated to one cycle of abrasion (z_{cycle}) is then assumed to be simply given by

$$z_{cycle} = h_{crater}/N_{cycles} \quad (5)$$

Uncertainties are approximately 15% of the result value. Depth profiles of positive ions, O^+, Na^+, Al^+, $^{28}Si^+$, and $^{29}Si^+$ were recorded, thanks to Bi_1^+ 25-keV, 1.2-pA beam for the analyses and O_2^+ 2-keV, 600-nA beams for the ablation.

The ion depth profiles are known to be artifactually broadened as a result of the instrumental resolution and because of the roughness of the reacted surface of the sample[37,45]. Therefore, the Al/^{28}Si and ^{29}Si/^{28}Si profiles from ToF-SIMS were deconvoluted following the method described in Daval et al.[45] in order to estimate the actual profile for the ratios of interest. See Supplementary Note 3.A for more details. The Al/^{28}Si profile was then used to define the altered-layer thickness and the $^{29}Si/^{28}Si$ profile was used to determine the average contribution of the solution in the composition of the altered layer following equation (A6) (see Supplementary Note 3.A).

Electron microscopy characterizations of the reacted surface. Scanning electron microscopy observations were conducted either with a Tescan VEGA II SEM operated at ITES (Strasbourg, France) or with a FEI Helios 600 Nanolab dual beam operated at CP2M (Marseille, France). The reacted samples after 33 days were then carbon-coated, and ultrathin electron-transparent cross sections were subsequently prepared by focused ion-beam (FIB) milling using the FEI Helios 600 Nanolab dual beam operated at CP2M (Marseille, France) following the methods previously described by Daval et al.[37]. In brief, FIB Ga^+ ion milling was carried out at an ion-beam voltage of 30 kV and beam currents ranging from 9 nA to 90 pA for the final steps. Micrometer-thick sections were lifted out in situ using an Omniprobe 200 micromanipulator and transferred to a half-copper grid for final ion milling to electron transparency (final thickness of ~100 nm). This milling was performed at a reduced acceleration voltage of 5 kV to reduce beam damage. For the same reasons, the final cleaning steps were then operated at 2 and 1 kV. The thin sections were oriented perpendicular to the striations at the surface of the crystals.

TEM and scanning transmission electron microscopy (STEM) observations were performed on FIB foils using a FEI Tecnaï G2 microscope operated at CP2M (Marseille, France) with a LaB_6 electron source operating at 200 kV. EDX spectra were acquired in STEM mode to probe the chemical composition of the interface between the altered layer and the substrate, with an Energy Dispersive X-ray Detector (Oxford XMax 80). The analyses were conducted on a total of four FIB thin sections (G1–2, C1–2, G3–2, and C3–2). The EDX maps were then processed as described in the Supplementary Note 3.B.

DATA AVAILABILITY

The authors declare that the data supporting the findings of this study are available on demand (benjamin.cagnon@univ-grenoble-alpes.fr)

Received: 30 August 2021; Accepted: 15 March 2022;
Published online: 21 April 2022

REFERENCES

1. Perez, A. et al. Comparing the reactivity of glasses with their crystalline equivalents: the case study of plagioclase feldspar. *Geochim. Cosmochim. Acta*. **254**, 122–141 (2019).
2. Huntington, T. et al. Calcium depletion in a southeastern United States forest ecosystem. *Soil Sci. Soc. Am. J.* **64**, 1845–1858 (2000).
3. Daval, D. Carbon dioxide sequestration through silicate degradation and carbon mineralisation: promises and uncertainties. *npj Mater. Degrad.* **2**, 11 (2018).
4. Grambow, B. Nuclear waste glasses - how durable? *Elements* **2**, 357–364 (2006).
5. Frankel, G. S. et al. Recent advances in corrosion science applicable to disposal of high-level nuclear waste. *Chem. Rev.* **121**, 12327–12383 (2021).
6. Gin, S., Delaye, J.-M., Angeli, F. & Schuller, S. Aqueous alteration of silicate glass: state of knowledge and perspectives. *npj Mater. Degrad.* **5**, 42 (2021).
7. Bunker, B. C. Molecular mechanisms for corrosion of silica and silicate-glasses. *J. Non Cryst. Solids* **179**, 300–308 (1994).
8. Jabraoui, H., Gin, S., Charpentier, T., Pollet, R. & Delaye, J.-M. Leaching and reactivity at the sodium aluminosilicate glass–water interface: insights from a ReaxFF molecular dynamics study. *J. Phys. Chem. C* **125**, 27170–27184 (2021).
9. Hou, X., Kirkpatrick, R. J., Struble, L. J. & Monteiro, P. J. M. Structural Investigations of Alkali Silicate Gels. *J. Am. Ceram. Soc.* **88**, 943–949 (2005).
10. Tambelli, C.E., Schneider, J. F., Hasparyk, N. P., Monteiro, P. J. M. Study of the structure of alkali–silica reaction gel by high-resolution NMR spectroscopy. *J. Non Cryst. Solids* **352**, 3429–3436 (2006).
11. Zhuravlev, L. T. The surface chemistry of amorphous silica. Zhuravlev model. *Colloids Surf. A Physicochem. Eng. Asp.* **173**, 1–38 (2000).
12. Zapol, P., He, H., Kwon, K. D. & Criscenti, L. J. First-principles study of hydrolysis reaction barriers in a sodium borosilicate glass. *Int. J. Appl. Glass Sci.* **4**, 395–407 (2013).
13. Inagaki, Y., Kikunaga, T., Idemitsu, K. & Arima, T. Initial dissolution rate of the international simple glass as a function of pH and temperature measured using microchannel flow-through test method. *Int. J. Appl. Glass Sci.* **4**, 317–327 (2013).
14. Ferrand, K., A. A. & Grambow, B. Water diffusion in the simulated French nuclear waste glass SON 68 contacting silica rich solutions: Experimental and modeling. *J. Nucl. Mater.* **355**, 54–67 (2006).
15. Collin, M., Fournier, M., Charpentier, T., Moskura, M. & Gin, S. Impact of alkali on the passivation of silicate glass. *npj Mater. Degrad.* **2**, 16 (2018).
16. Vienna, J. D., Ryan, J. V., Gin, S. & Inagaki, Y. Current understanding and remaining challenges in modeling long-term degradation of borosilicate nuclear waste glasses. *Int. J. Appl. Glass Sci.* **4**, 283–294 (2013).
17. Grambow, B. & Muller, R. First-order dissolution rate law and the role of surface layers in glass performance assessment. *J. Nucl. Mater.* **298**, 112–124 (2001).
18. Rebiscoul, D. et al. Morphological evolution of alteration layers formed during nuclear glass alteration: new evidence of a gel as a diffusive barrier. *J. Nucl. Mater.* **326**, 9–18 (2004).
19. Diane Rebiscoul, P. F., Stéphane Gin & André Ayral Protective properties and dissolution ability of the gel formed during nuclear glass alteration. *J. Nucl. Mater.* **342**, 26–34 (2005).
20. Gin, S., Ribet, I. & Couillard, M. In *International Topical Workshop on Glass in its Disposal Environment*. 1–10 (Elsevier Science Bv) (2000).
21. Valle, N. et al. Elemental and isotopic (29Si and 18O) tracing of glass alteration mechanisms. *Geochim. Cosmochim. Acta* **74**, 3412–3431 (2010).
22. Gin, S. et al. Dynamics of self-reorganization explains passivation of silicate glasses. *Nat. Commun.* **9**, 2169 (2018).
23. Cailleteau, C. et al. Insight into silicate-glass corrosion mechanisms. *Nat. Mater.* **7**, 978–983 (2008).
24. Casey, W. H. Glass and mineral corrosion dynamics and durability. *Nat. Mater.* **7**, 930–932 (2008).
25. Jollivet, P. et al. Investigation of gel porosity clogging during glass leaching. *J. Non Cryst. Solids* **354**, 4952–4958 (2008).
26. Bourcier, W. L., Peiffer, D. W., Knauss, K. G., McKeegan, K. D. & Smith, D. K. A kinetic model for borosilicate glass dissolution based on the dissolution affinity of a surface alteration layer. *MRS Online Proc. Libr. Arch.* **176**, null-null (1989).
27. Gin, S. et al. Insights into the mechanisms controlling the residual corrosion rate of borosilicate glasses. *npj Mater. Degrad.* **4**, 1–9 (2020).
28. Ojovan, M. I., Pankov, A. & Lee, W. E. The ion exchange phase in corrosion of nuclear waste glasses. *J. Nucl. Mater.* **358**, 57–68 (2006).
29. Frugier, P. et al. SON68 nuclear glass dissolution kinetics: Current state of knowledge and basis of the new GRAAL model. *J. Nucl. Mater.* **380**, 8–21 (2008).
30. Fournier, M., Gin, S. & Frugier, P. Resumption of nuclear glass alteration: state of the art. *J. Nucl. Mater.* **448**, 348–363 (2014).
31. Ribet, S. & Gin, S. Role of neoformed phases on the mechanisms controlling the resumption of SON68 glass alteration in alkaline media. *J. Nucl. Mater.* **324**, 152–164 (2004).
32. Ebert, W. L. & Bates, J. K. A comparison of glass reaction at high and low glass surface/solution volume. *Nucl. Technol.* **104**, 372–384 (1993).
33. Van Iseghem, P. & Grambow, B. The long-term corrosion and modelling of two simulated belgian reference high-level waste glasses. *MRS Proc.* **112**, 631 (1987).
34. Petit, J. C., Dellamea, G., Dran, J. C., Schott, J. & Berner, R. A. Mechanism of diopside dissolution from hydrogen depth profiling. *Nature* **325**, 705–707 (1987).
35. Hellmann, R. The albite-water system: part 4. Diffusion modeling of leached and hydrogen-enriched layers. *Geochim. Cosmochim. Acta* **61**, 1595–1611 (1997).
36. Hellmann, R., Dran, J. C. & DellaMea, G. The albite-water system: part 3. Characterization of leached and hydrogen-enriched layers formed at 300 degrees C using MeV ion beam techniques. *Geochim. Cosmochim. Acta* **61**, 1575–1594 (1997).
37. Hellmann, R., Penisson, J.-M., Hervig, R. L., Thomassin, J.-H. & Abrioux, M.-F. An EFTEM/HRTEM high-resolution study of the near surface of labradorite feldspar altered at acid pH: evidence for interfacial dissolution-reprecipitation. *Phys. Chem. Miner.* **30**, 192–197 (2003).
38. Daval, D. et al. Mechanism of wollastonite carbonation deduced from micro- to nanometer length scale observations. *Am. Miner.* **94**, 1707–1726 (2009).
39. Hellmann, R. et al. Unifying natural and laboratory chemical weathering with interfacial dissolution–reprecipitation: A study based on the nanometer-scale chemistry of fluid–silicate interfaces. *Chem. Geol.* **294–295**, 203–216 (2012).
40. Geisler, T. et al. Aqueous corrosion of borosilicate glass under acidic conditions: a new corrosion mechanism. *J. Non Cryst. Solids* **356**, 1458–1465 (2010).
41. Ruiz-Agudo, E., Putnis, C. V., Rodriguez-Navarro, C. & Putnis, A. Mechanism of leached layer formation during chemical weathering of silicate minerals. *Geol* **40**, 947–950 (2012).
42. Ruiz-Agudo, E. et al. Control of silicate weathering by interface-coupled dissolution-precipitation processes at the mineral-solution interface. *Geology* **44**, 567–570 (2016).
43. Putnis, A. Mineral replacement reactions. *Rev. Mineral. Geochem.* **70**, 87–124 (2009).
44. Putnis, A. Why mineral interfaces matter. *Sci* **343**, 1441–1442 (2014).
45. Daval, D. et al. Dynamics of altered surface layer formation on dissolving silicates. *Geochim. Cosmochim. Acta* **209**, 51–69 (2017).
46. Hellmann, R. et al. Nanometre-scale evidence for interfacial dissolution–reprecipitation control of silicate glass corrosion. *Nat. Mater.* **14**, 307–311 (2015).
47. Gin, S. et al. Atom-probe tomography, TEM and ToF-SIMS study of borosilicate glass alteration rim: a multiscale approach to investigating rate-limiting mechanisms. *Geochim. Cosmochim. Acta.* **202**, 57–76 (2017).
48. Gin, S. et al. A general mechanism for gel layer formation on borosilicate glass under aqueous corrosion. *J. Phys. Chem. C* **124**, 5132–5144 (2020).
49. Wild, B. et al. pH-dependent control of feldspar dissolution rate by altered surface layers. *Chem. Geol.* **442**, 148–159 (2016).
50. Gin, S. et al. Origin and consequences of silicate glass passivation by surface layers. *Nat. Commun.* **6**, 6360 (2015).
51. Gin, S., Ryan, J. V., Schreiber, D. K., Neeway, J. & Cabié, M. Contribution of atom-probe tomography to a better understanding of glass alteration mechanisms: application to a nuclear glass specimen altered 25 years in a granitic environment. *Chem. Geol.* **349–350**, 99–109 (2013).
52. Bouakkaz, R., Abdelouas, A., El Mendili, Y., Grambow, B. & Gin, S. SON68 glass alteration under Si-rich solutions at low temperature (35–90 °C): kinetics, secondary phases and isotopic exchange studies. *RSC Adv.* **6**, 72616–72633 (2016).
53. Stillings, L. L. & Brantley, S. L. Feldspar dissolution at 25 °C and pH 3: reaction stoichiometry and the effect of cations. *Geochim. Cosmochim. Acta* **59**, 1483–1496 (1995).
54. Hopf, J. et al. Toward an understanding of surface layer formation, growth, and transformation at the glass–fluid interface. *Geochim. Cosmochim. Acta* **229**, 65–84 (2018).
55. Fournier, M. et al. Glass dissolution rate measurement and calculation revisited. *J. Nucl. Mater.* **476**, 140–154 (2016).
56. Pollet-Villard, M. et al. Does crystallographic anisotropy prevent the conventional treatment of aqueous mineral reactivity? A case study based on K-feldspar dissolution kinetics. *Geochim. Cosmochim. Acta* **190**, 294–308 (2016).
57. Lee, M. R., Hodson, M. E. & Parsons, I. The role of intragranular microtextures and microstructures in chemical and mechanical weathering: direct comparisons of experimentally and naturally weathered alkali feldspars. *Geochim. Cosmochim. Acta* **62**, 2771–2788 (1998).

58. Worden, R. H., Walker, F. D. L., Parsons, I. & Brown, W. L. Development of microporosity, diffusion channels and deuteric coarsening in perthitic alkali feldspars. *Contrib. Mineral. Petrol.* **104**, 507–515 (1990).
59. Fournier, M. et al. Effect of pH on the stability of passivating gel layers formed on International Simple Glass. *J. Nucl. Mater.* **524**, 21–38 (2019).
60. Verney-Carron, A. et al. Understanding the mechanisms of Si–K–Ca glass alteration using silicon isotopes. *Geochim. Cosmochim. Acta* **203**, 404–421 (2017).
61. Daval, D. et al. Influence of amorphous silica layer formation on the dissolution rate of olivine at 90 degrees C and elevated pCO(2). *Chem. Geol.* **284**, 193–209 (2011).
62. Kurganskaya, I. & Luttge, A. A comprehensive stochastic model of phyllosilicate dissolution: structure and kinematics of etch pits formed on muscovite basal face. *Geochim. Cosmochim. Acta* **120**, 545–560 (2013).
63. Xiao, Y. & Lasaga, A. C. Ab initio quantum mechanical studies of the kinetics and mechanisms of silicate dissolution: H+(H3O+) catalysis. *Geochim. Cosmochim. Acta* **58**, 5379–5400 (1994).
64. Damodaran, K., Delaye, J.-M., Kalinichev, A. G. & Gin, S. Deciphering the non-linear impact of Al on chemical durability of silicate glass. *Acta Mater.* **225**, 117478 (2022).
65. Pierce, E. et al. Experimental determination of the effect of the ratio of B/Al on glass dissolution along the nepheline (NaAlSiO 4)–malinkoite (NaBSiO 4) join. *Geochim. Cosmochim. Acta* **74**, 2634–2654 (2010).
66. Hamilton, J. P., Brantley, S. L., Pantano, C. G., Criscenti, L. J. & Kubicki, J. D. Dissolution of nepheline, jadeite and albite glasses: toward better models for aluminosilicate dissolution. *Geochim. Cosmochim. Acta* **65**, 3683–3702 (2001).
67. Stone-Weiss, N. et al. An insight into the corrosion of alkali aluminoborosilicate glasses in acidic environments. *Phys. Chem. Chem. Phys.* **22**, 1881–1896 (2020).
68. Hamilton, J. P., Pantano, C. G. & Brantley, S. L. Dissolution of albite glass and crystal. *Geochim. Cosmochim. Acta* **64**, 2603–2615 (2000).
69. Yang, Y., Min, Y. & Jun, Y.-S. A mechanistic understanding of plagioclase dissolution based on Al occupancy and T–O bond length: from geologic carbon sequestration to ambient conditions. *Phys. Chem. Chem. Phys.* **15**, 18491–18501 (2013).
70. Brantley, S. L. & Olsen, A. A. *Treatise on Geochemistry (Second Edition)* (ed. Turekian, K. K.) 69–113 (Elsevier, 2014).
71. Iler, R. K. *The chemistry of silica: solubility, polymerization, colloid and surface properties, and biochemistry/Ralph K. Iler*. (Wiley, 1979)

ACKNOWLEDGEMENTS

The authors thank Gilles Morvan (ITES), Thierry Perrone (ITES), and René Boutin (ITES) for performing EBSD, providing advice and help for the experiments, and helping with ICP–AES and ICP-MS measurements, respectively. The authors are also grateful to Loan Lai, Elodie Chauvet, Amandine David, and Yves Depuydt from Tescan Analytics for performing ToF-SIMS analyses and operating one FIB thin section. Nicolas Michau and Christelle Martin are thanked for their inputs on an earlier version of this paper. This work was funded by Andra and EDF.

AUTHOR CONTRIBUTIONS

B.C. performed the experiments and analyzed data. M.C. prepared FIB thin sections, performed, and analyzed the TEM measurements. D.L. contributed to design the alkali-fusion and cation-exchange column protocols. D.D. and S.G. analyzed data and supervised the research. B.C., D.D., and S.G. wrote the paper, with contributions from all authors.

COMPETING INTERESTS

The authors declare no competing interests.

ADDITIONAL INFORMATION

Supplementary information The online version contains supplementary material available at https://doi.org/10.1038/s41529-022-00240-6.

Correspondence and requests for materials should be addressed to Benjamin Cagnon.

Reprints and permission information is available at http://www.nature.com/reprints

Publisher's note Springer Nature remains neutral with regard to jurisdictional claims in published maps and institutional affiliations.